Astronomy & Astrophysics manuscript no. MVerma_A_A
May 25, 2016
©ESO 2016

arXiv:1605.07462v1 [astro-ph.SR] 24 May 2016

Horizontal flow fields in and around a small active region

The transition period between flux emergence and decay

M. Verma[1], C. Denker[1], H. Balthasar[1], C. Kuckein[1], S.J. González Manrique[1,2], M. Sobotka[3], N. Bello González[4], S. Hoch[4], A. Diercke[1,2], P. Kummerow[1,2], T. Berkefeld[4], M. Collados[5], A. Feller[6], A. Hofmann[1], F. Kneer[7], A. Lagg[6], J. Löhner-Böttcher[4], H. Nicklas[7], A. Pastor Yabar[5,10], R. Schlichenmaier[4], D. Schmidt[8], W. Schmidt[4], M. Schubert[4], M. Sigwarth[4], S.K. Solanki[6,9], D. Soltau[4], J. Staude[1], K.G. Strassmeier[1], R. Volkmer[4], O. von der Lühe[4], and T. Waldmann[4]

[1] Leibniz-Institut für Astrophysik Potsdam (AIP), An der Sternwarte 16, 14482 Potsdam, Germany, mverma@aip.de
[2] Universität Potsdam, Institut für Physik und Astronomie, Karl-Liebknecht-Straße 24/25, 14476 Potsdam-Golm, Germany
[3] Astronomical Institute, Academy of Sciences of the Czech Republic, Fričova 298, 25165 Ondřejov, Czech Republic
[4] Kiepenheuer-Institut für Sonnenphysik, Schöneckstr. 6, 79104 Freiburg, Germany
[5] Instituto de Astrofísica de Canarias, C/ Vía Láctea s/n, 38205 La Laguna, Tenerife, Spain
[6] Max-Planck-Institut für Sonnensystemforschung, Justus-von-Liebig-Weg 3, 37077 Göttingen, Germany
[7] Institut für Astrophysik, Georg-August-Universität Göttingen, Friedrich-Hund-Platz 1, 37077 Göttingen, Germany
[8] National Solar Observatory, 3010 Coronal Loop Sunspot, NM 88349, USA
[9] School of Space Research, Kyung Hee University,Yongin, Gyeonggi-Do, 446-701, Republic of Korea
[10] Dept. Astrofísica, Universidad de La Laguna, E-38205, La Laguna, Tenerife, Spain

submitted 25/02/2016, accepted 12/05/2016

ABSTRACT

Context. The solar magnetic field is responsible for all aspects of solar activity. Thus, emergence of magnetic flux at the surface is the first manifestation of the ensuing solar activity.
Aims. Combining high-resolution and synoptic observations aims to provide a comprehensive description of flux emergence at photospheric level and of the growth process that eventually leads to a mature active region.
Methods. The small active region NOAA 12118 emerged on 2014 July 17 and was observed one day later with the 1.5-meter GREGOR solar telescope on 2014 July 18. High-resolution time-series of blue continuum and G-band images acquired in the blue imaging channel (BIC) of the GREGOR Fabry-Pérot Interferometer (GFPI) were complemented by synoptic line-of-sight magnetograms and continuum images obtained with the Helioseismic and Magnetic Imager (HMI) onboard the Solar Dynamics Observatory (SDO). Horizontal proper motions and horizontal plasma velocities were computed with local correlation tracking (LCT) and the differential affine velocity estimator (DAVE), respectively. Morphological image processing was employed to measure the photometric and magnetic area, magnetic flux, and the separation profile of the emerging flux region during its evolution.
Results. The computed growth rates for photometric area, magnetic area, and magnetic flux are about twice as high as the respective decay rates. The space-time diagram using HMI magnetograms of five days provides a comprehensive view of growth and decay. It traces a leaf-like structure, which is determined by the initial separation of the two polarities, a rapid expansion phase, a time when the spread stalls, and a period when the region slowly shrinks again. The separation rate of 0.26 km s^{-1} is highest in the initial stage, and it decreases when the separation comes to a halt. Horizontal plasma velocities computed at four evolutionary stages indicate a changing pattern of inflows. In LCT maps we find persistent flow patterns such as outward motions in the outer part of the two major pores, a diverging feature near the trailing pore marking the site of upwelling plasma and flux emergence, and low velocities in the interior of dark pores. We detected many elongated rapidly expanding granules between the two major polarities, with dimensions twice as large as the normal granules.

Key words. Sun: photosphere – Sun: surface magnetism – Techniques: image processing – Methods: data analysis

1. Introduction

Solar activity is directly related to the Sun's magnetic field. Flux emergence affects all atmospheric layers and involves many coupled but diverse physical environments. The rise of buoyant magnetic flux tubes from the convection zone to the surface and higher solar atmospheric layers eventually leads to the formation of sunspots and active regions (Parker 1955; Zwaan 1978). The rising flux tubes are already concentrated bundles of magnetic field lines when they penetrate the photosphere. Zwaan (1985) explained the general dynamics of emerging flux regions (EFRs), that is, the separation of opposite polarities and coalescence of same-polarity magnetic features by the buoyancy of (collapsed) flux tubes.

Typically, EFRs consist of many pores and protopores in various stages of growth or decay with separating polarities and sometimes with strong photospheric shear flows (Brants & Steenbeek 1985). The properties and dynamics of small-scale magnetic structures within an EFR were thoroughly examined by Strous et al. (1996) and Strous & Zwaan (1999). They found thread-like concentrations of magnetic flux in facular elements within an EFR. Flux emergence occurred throughout the region,

which was governed by the separation of opposite polarities with a velocity of about 1 km s^{-1}.

The vector magnetic field in and around an EFR was studied by Lites et al. (1998). Their observations were in accordance with earlier ideas of emerging bipolar flux, that is, the buoyant flux tubes transport mass from the photosphere to the chromosphere, and subsequently material drains down to footpoints along arched magnetic loops. These authors concluded that the formation of pores or sunspots by coalescence of magnetic flux has its origin in the emergence of subsurface structures. This picture was confirmed and further elaborated by Solanki (2003) and Xu et al. (2010), who determined the magnetic and velocity structure of EFRs in both the photosphere and the chromosphere from the Si I 10827 and the He I 10830Å lines. The strength of the magnetic field in young EFRs is weak (< 500 G). The magnetic field becomes stronger (> 500 G) and vertical within half a day after emergence. Additionally, the filling factor decreases from about 80% to 40% (Kubo et al. 2003). Spectropolarimetric observations presented by Watanabe et al. (2008) of an EFR in the Fe I 630.2 nm spectral region together with Hα filtergrams showed that magnetic flux emergence was associated with the appearance of Ellerman bombs. The complex velocity and magnetic fields of EFRs were the focus of a study by Luoni et al. (2011). They found global magnetic twist during the emergence phase in a sample of 40 active regions using elongated 'magnetic tongues' (López Fuentes et al. 2000) as a proxy for the magnetic helicity.

The interaction of rising flux with photospheric plasma during and after emergence is one aspect of the EFR evolution. The separation of opposite polarities is often observed (Brants & Steenbeek 1985), and horizontal flows play a significant role in the growth of EFRs. Otsuji et al. (2011) inferred horizontal velocities, modes of emergence, and total magnetic flux of 101 flux emergence events using Hinode data. They found converging as well as diverging flows in various emerging events. The computed growth of magnetic flux, separation of two polarities, and velocity of separation followed power laws. Otsuji et al. (2011) obtained a physical description of flux emergence, where buoyant emerging magnetic fields evolve in balance with the surrounding turbulent atmosphere. Toriumi et al. (2012) detected horizontal divergent flows prior to flux emergence using Helioseismic and Magnetic Imager (HMI) dopplergrams and magnetograms. These flows are caused by plasma escaping horizontally from the rising flux announcing a newly emerging active region. In addition, horizontal flows separating positive and negative polarities are higher in the beginning but decrease over time. Isolated flux emergence, that is, outside of pre-existing magnetic fields, was analyzed by Centeno (2012), also using Solar Dynamics Observatory (SDO) observations. She noted that EFRs start as simple magnetic bipolar regions growing by merging of various small magnetic features along with systematic downflows at the footpoints.

The magnetohydrodynamic (MHD) simulations of Cheung et al. (2010) reproduced observational properties of flux emergence such as elongated granules, mixed polarity patterns in the emerging flux region, and pore formation. They kinematically advected a magnetic semi-torus upward from a depth of 7.5 Mm to the photosphere. Stein et al. (2011) simulated flux emergence using the rise and evolution of untwisted horizontal flux with the same entropy as the nonmagnetized ascending plasma, which was carried by upflows from a depth of 20 Mm. Rempel & Cheung (2014) expanded the work of Cheung et al. (2010) and included the emergence and evolution of buoyant flux tubes. In their work, the flux is able to emerge to the photosphere even in the absence of twist.

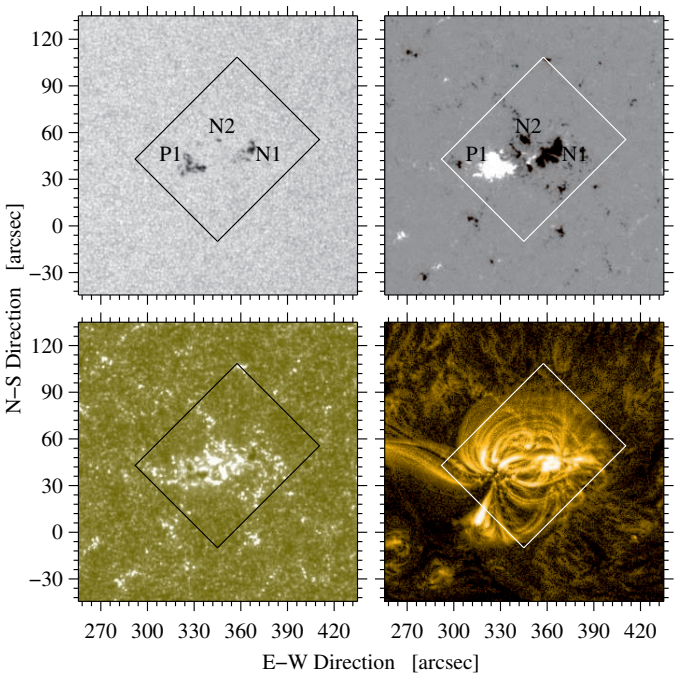

Fig. 1. Overview of active region NOAA 12118: HMI continuum image (*top left*), HMI magnetogram (*top right*), AIA λ160 nm image (*bottom left*), and AIA Fe IX λ17.1 nm image (*bottom right*) observed on 2014 July 18 at 08:00 UT. A bipolar EFR appeared on 2014 July 17 to the west of the central meridian in the northern hemisphere. Observations of active region NOAA 12118 started at 08:00 UT and ended at 10:40 UT on 2014 July 18. The rectangle is the FOV covered by GREGOR high-spatial resolution data. The two major pores and one smaller pore are marked as P1, N1, and N2 to aid discussions in Sect. 3.3

Collectively, various observational studies and numerical simulations present a physical description of flux emergence on the solar surface. However, high-resolution observations of the solar surface are needed to enhance our understanding of the complex interaction between horizontal flows and magnetic fields during the process of flux emergence. In the current study, we present the first analysis of observations made with the GREGOR solar telescope, taken during a 50-day early science campaign in 2014 July – August.

2. Observations and data reduction

2.1. Observations

Newly emerging flux was observed with GREGOR Fabry-Pérot Interferometer (GFPI) / blue imaging channel (BIC) (Denker et al. 2010; Puschmann et al. 2012) at the 1.5-meter GREGOR solar telescope (Denker et al. 2012; Schmidt et al. 2012) on 2014 July 18 starting at 07:56 UT. The GFPI was originally developed by the Institute for Astrophysics in Göttingen (Bendlin et al. 1992; Puschmann et al. 2006; Bello González & Kneer 2008). The emerging bipolar region was labeled active region NOAA 12118 on the next day. The image quality was improved in real-time by the GREGOR adaptive pptics system (GAOS, Berkefeld et al. 2010, 2012), which locked on a small, circular pore in the center of the active region located in between the pair of clustered, opposite-polarity pores.

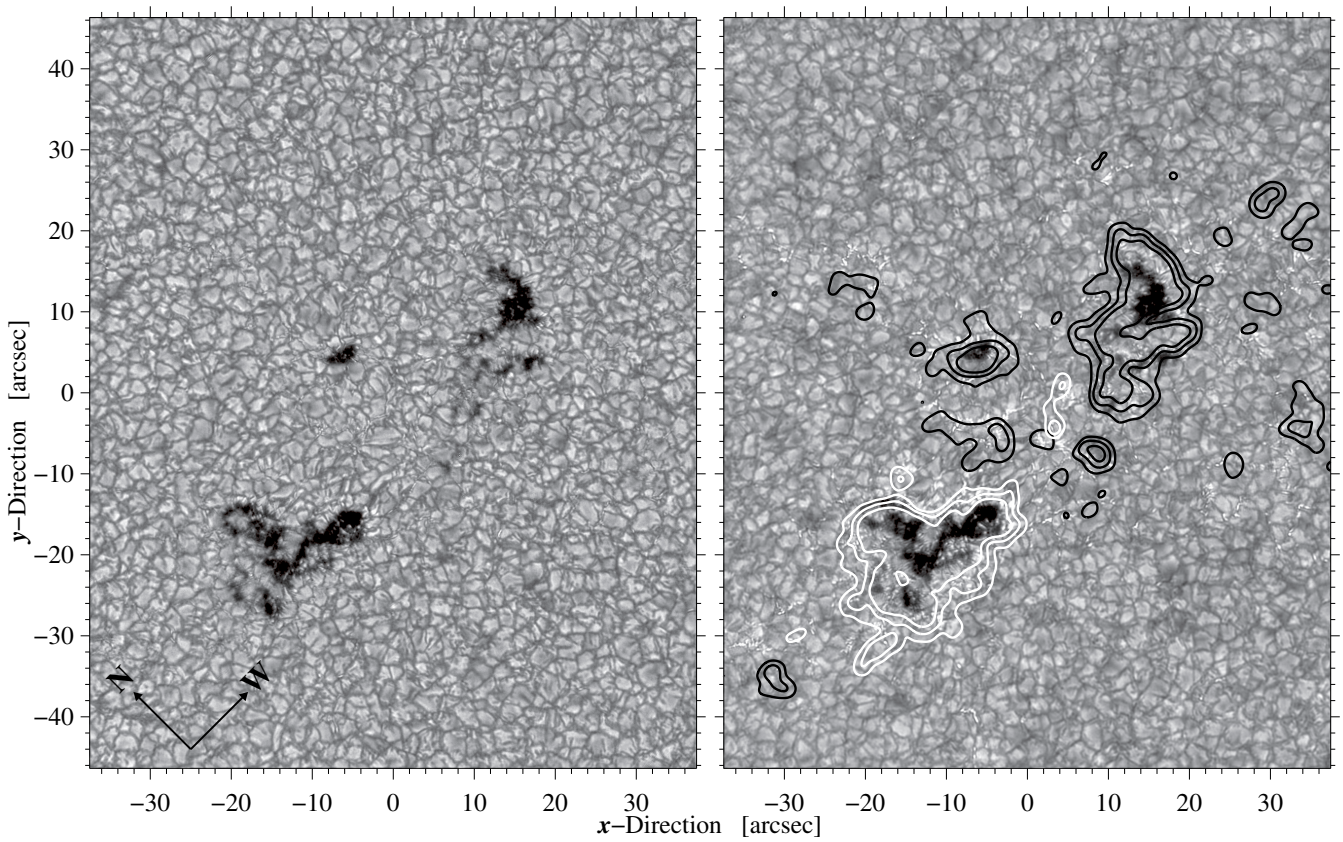

Fig. 2. Blue continuum (*left*) and G-band (*right*) images of the time-series observed on 2014 July 18 at 08:46 UT and 08:43 UT, respectively. Images were restored with KISIP. The two images are scaled between 0.4 and 1. The black and white contours superposed on the G-band image are created using a HMI magnetogram displayed at levels ±100, ±250, and ±500 G. The north and west directions are indicated by the arrows in the lower left corner.

The blue continuum observations λ450.6 nm were split into four 30-minute time-series with 60 image sequences containing 80 images each with an exposure time of 4 ms, which are appropriate for image restoration. The four time-series started at 07:56 UT, 08:36 UT, 09:13 UT, and 10:09 UT, respectively. The image scale of 0.035 ″ pixel^{-1} for the 2160×2672-pixel images leads to a field-of-view (FOV) of 75″ × 93″ covering the entire region and the complex flow field associated with the growing and separating regions of opposite magnetic polarity. The cadence of 30 s for the time-series of restored blue continuum images is ideally suited for horizontal flow measurements (Verma & Denker 2011). Auxiliary G-band images λ430.7 nm were also taken but camera problems prevented us from taking continuous time-series. However, in some cases the time-series were of sufficient duration to allow us tracking G-band brightenings, which are often associated with small-scale magnetic flux elements (Uitenbroek & Tritschler 2006; Leenaarts et al. 2006). The best images of the restored blue continuum and G-band time-series are featured in Fig. 2. The black arrows show the orientation of the BIC FOV on the solar disk at the given time. However, the altitude-azimuth mount of the telescope (Volkmer et al. 2012) introduces an image rotation, that has to be taken into account when analyzing time-series.

The observed active region NOAA 12118 started emerging on July 17 around 15:00 UT at N7° W41° (disk-center coordinates) and was categorized as an $\alpha\beta$-group according to the Hale classification (Hale et al. 1919). At the time of the GREGOR observations on July 18, the region attained its maximum size. By July 19 the region started to fade out, and by July 22 it had decayed significantly before rotating off the visible disk. Although C-class flare activity was predicted (Gallagher et al. 2002), the region did not produce any noteworthy flare.

The temporal evolution of the magnetic flux is based on full-disk continuum images and line-of-sight (LOS) magnetograms of HMI (Schou et al. 2012; Couvidat et al. 2012; Wachter et al. 2012) onboard SDO (Scherrer et al. 2012). To appraise the active region in higher atmospheric layers, we used an Fe IX image λ17.1 nm of the Atmospheric Imaging Assembly (AIA, Lemen et al. 2012). We improved the contrast of this image using noise adaptive fuzzy equalization (NAFE, Druckmüller 2013). Figure 1 gives an overview of active region NOAA 12118. The black and white rectangular boxes represent the FOV observed by GREGOR/BIC.

2.2. Data reduction

The blue continuum and G-band images were restored using the Kiepenheuer Institute speckle interferometry package (KISIP, Wöger et al. 2008; Wöger & von der Lühe 2008). In this code the image restoration is performed in the Fourier domain. The code separates the Fourier phases of the images from their amplitudes. Fourier phases can be retrieved by two different phase reconstruction algorithms: by the Knox-Thompson (Knox & Thompson 1974) and triple-correlation (Weigelt & Wirnitzer 1983), whereas Fourier amplitudes are reconstructed independently (Labeyrie 1970). Figure 2 shows images reconstructed with the triple-correlation technique. The image contrast, de-

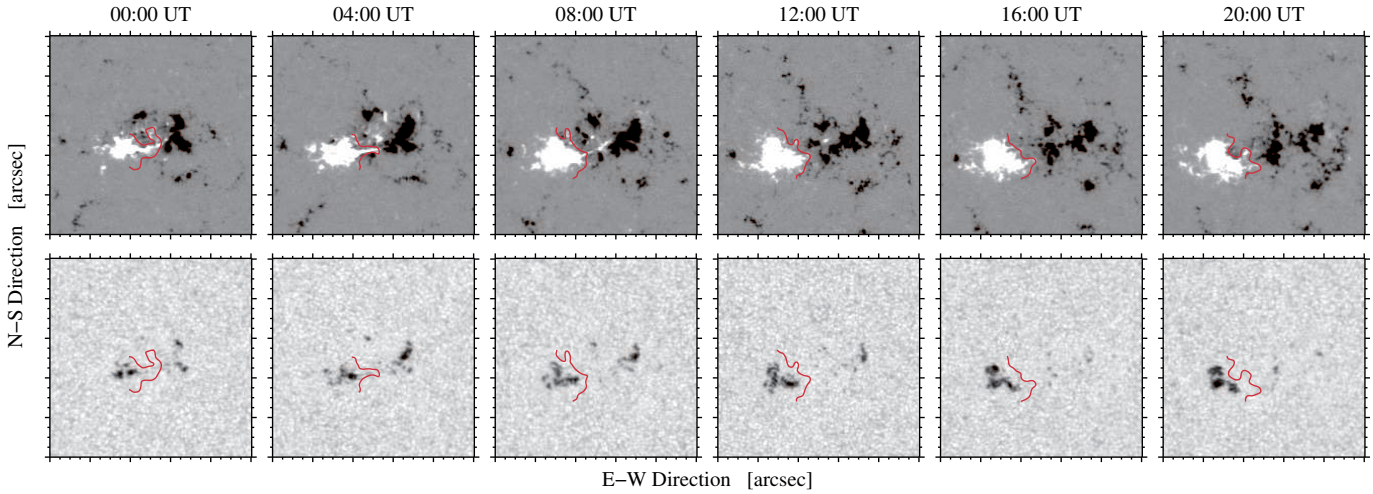

Fig. 3. Pores belonging to active region NOAA 12118 were visible on the solar surface for about four days (2014 July 17 – 20). Cutouts of HMI magnetograms and continuum images (100″ × 100″) show the temporal evolution of the region at four-hour intervals centered on the time of the GREGOR observations, that is, 08:00 UT on July 18. The magnetograms are displayed between ±250 G. The red line marks the magnetic neutral line at the respective time.

graded by scattered light, was then restored using the method described in Bello González & Kneer (2008).

We applied LCT (for details see Verma & Denker 2011; Verma et al. 2013) to the blue continuum image sequences to compute horizontal flows. The restored time-series is aligned (image rotation and image displacement) with sub-pixel accuracy with respect to the average image of the time-series, and the signature of five-minute oscillation was removed using a subsonic Fourier filter with a cut-off velocity corresponding to the photospheric sound speed. The LCT technique computes cross-correlations over 48×48-pixel image tiles with a Gaussian kernel having a FWHM = 1200 km corresponding to the typical size of a granule. The time cadence was Δt = 60 s, and the flow maps were averaged over ΔT = 30 min.

We chose from the SDO/HMI database one continuum image and LOS magnetogram with 4096 × 4096 pixels every hour for the period from 2014 July 17 – 22, which is a total of 120 full-disk images and magnetograms. The image scale is in both cases about 0.5″ pixel^{-1}. The continuum images were corrected for limb-darkening to produce contrast-enhanced images (see e.g., Denker et al. 1999). The magnetic and photometric evolution of the active region on July 18 is shown in Fig. 3. The magnetic flux values were corrected for projection effects assuming that all flux tubes are perpendicular to the solar surface.

We selected four different time sequences of HMI LOS magnetograms with a cadence of 45 s to study the magnetic field evolution of the region and to compute horizontal plasma velocities. The selected time sequences were from 15:30 – 17:30 UT on July 17, from 08:00 – 10:00 UT on July 18, from 00:00 – 02:00 UT on July 19, and from 21:30 – 23:30 UT on July 19. The basic calibration included dark and flat-field corrections, elimination of spikes, and removal of geometric foreshortening. In the next step, we applied DAVE (Schuck 2005, 2006) to the magnetogram sequence to retrieve the horizontal plasma velocities. The underlying physics is based on magnetic induction equation, and the implementation of DAVE implies an affine velocity profile. The horizontal flows were estimated using temporal and spatial derivatives of the magnetic field. We applied the Scharr operator (Scharr 2007) for the spatial derivatives and a five-point stencil with a time difference of 15 min between neighboring magnetograms for the temporal derivative. The horizontal plasma velocities depicted in Fig. 6 are averages of 80 individual DAVE maps covering one hour. However, the temporal derivatives add 30 min before and after this time interval so that the horizontal plasma velocities contain information from a two-hour period. We employed DAVE because it provides more accurate results than applying LCT to magnetograms (Schuck 2005, 2006).

3. Results

In the following sections, we present the main results of this study. Starting with the temporal evolution of the region size and magnetic flux contents, we discuss horizontal plasma velocities computed using DAVE, and we study changes in horizontal proper motions.

3.1. Photometric and magnetic evolution

The emerging flux region appeared on the solar disk at about 15:00 UT on July 17. The EFR surfaced in a quiet-Sun region without any major active region in the vicinity. The bipolar region started out with two pores. The two major pores were eventually joined by smaller pores of both polarities. The region was fully developed by the time of the GREGOR observations. Both main pores were increasing in area, and the separation between them grew as well. Snapshots of the region's evolution are shown for July 18 in Fig. 3. The HMI continuum images and LOS magnetograms are displayed every four hours. We grouped these snapshots into three phases: (1) growth phase 00:00 – 04:00 UT, (2) maximum phase 08:00 – 12:00 UT, and (3) decay phase 16:00 – 20:00 UT. In phase (1) the leading part with negative polarity consists of two smaller pores, and another small pore of the same polarity is developing in the center of the FOV. The trailing part is more compact at 00:00 UT, in contrast to the typical appearance of active regions. By phase (2), both leading and trailing parts have grown. The leading polarity started to dissolve at 12:00 UT, as is evident in the continuum image, while the trailing part continues to grow in area. After four hours in phase (3), any traces of the leading polarity have vanished in the continuum images, but the trailing part continues to increase in area even until 20:00 UT.

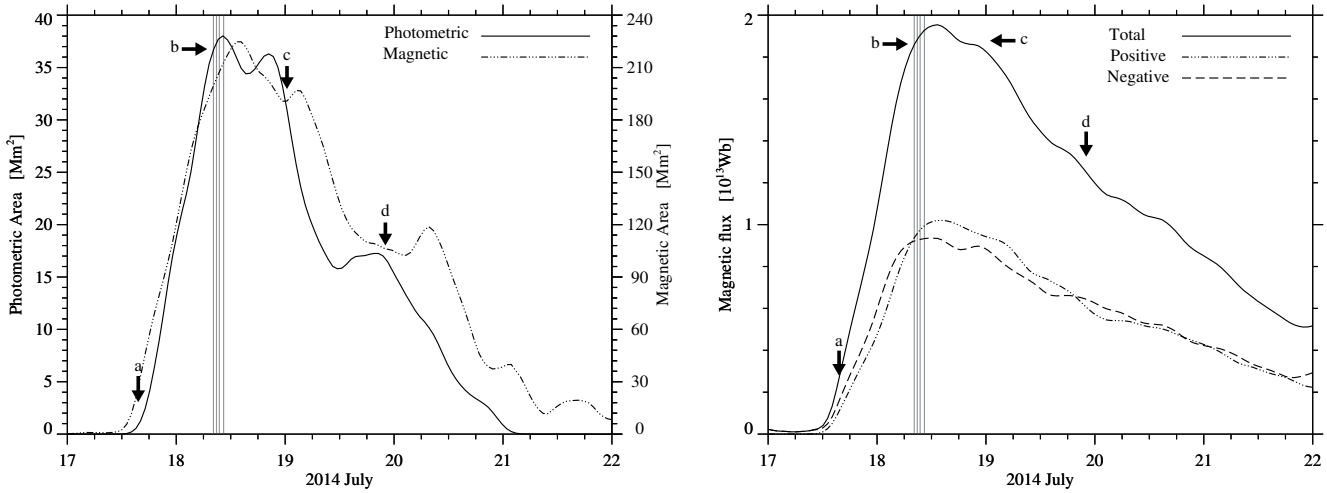

Fig. 4. Temporal evolution of the area (*left*) and magnetic flux (*right*) in active region NOAA 12118 during its disk passage. The solid and dash-dotted lines in the left panel show the photometric and magnetic area, respectively. The solid, dash-dotted, and dashed lines in the right panel correspond to the total, positive, and negative magnetic flux, respectively. The four vertical lines indicate the time of the BIC time-series. The labels a to d indicate different stages of active region evolution, which are explained in Sect. 3.2.

After July 18, the region decayed significantly. Over the course of their evolution, the pores never developed a penumbra, that is, the active region never evolved into a group with sunspots. As already mentioned, the leading pores dissolved first, while the trailing pores became more compact. The second phase of flux emergence after the appearance of two polarities is the coalescence of small-scale magnetic flux elements (Strous & Zwaan 1999; Centeno 2012), which we also observed in this region. Although the region had two main pores of opposite polarity, the magnetic neutral line was initially complex, but became simpler with time. Initially, a tongue of positive polarity extended into the negative-polarity territory. Then, the central part of the active region exhibited mixed polarity. Finally, the opposite polarities were clearly separated. No arch filament structure was present in Hα full-disk images obtained with the Chromospheric Telescope (ChroTel, Kentischer et al. 2008; Bethge et al. 2011), instead, the region contained bright plage with only a single filament connecting the two opposite polarities.

We used the contrast-enhanced HMI full-disk continuum images and LOS magnetograms to follow the photometric and magnetic evolution of the region over five days. The overall evolution of area and flux contained in the active region are shown in Fig. 4. The dark pores were identified with the help of intensity thresholding and morphological image processing. We used a fixed intensity threshold of $I = 0.8I_0$, where I_0 refers to the normalized quiet-Sun intensity. We took the measured magnetic field strength at face value and only carried out a geometrical correction to yield the proper average values of the magnetic flux. We use the term magnetic field strength throughout the text to refer to the longitudinal flux. To compute the temporal evolution of the magnetic flux, we created a binary template that only contains pixels above or below ±50 Gauss in the HMI magnetograms. Morphological erosion with a kernel of 1 Mm was applied to the template three times to eliminate small isolated flux concentrations. Finally, we used morphological dilation with a kernel of 5 Mm to include the strong magnetic fields in the immediate neighborhood of the active region. This corresponds to a modified morphological opening operation.

We used linear regression to compute the growth and decay rates. A linear fit to the HMI continuum data is appropriate because there is no indication for a parabolic (or any other nonlinear) growth or decay law. There are two peaks on July 18, best visible in the photometric area record, but also weakly seen in the total flux, one around the time of the GREGOR observations 10:28 UT and another at 20:36 UT. The second peak arises because of the still growing, trailing part of the region. However, at the same time, the leading part had already entirely dissolved. We computed only one growth rate, namely from the start of the growth phase to just before the first peak. The photometric growth rate for the area is 46.6 Mm^2 day^{-1}. The decay of the photometric area of the region also occurs in two stages. The two local maxima during the decay phase lead to two decay rates. First the region decays rapidly at a rate of 23.5 Mm^2 day^{-1}, which is comparable to the growth rate. Starting on July 20, it decays more slowly at 13.9 Mm^2 day^{-1}, and by July 21 the photometric imprint of the region has completely vanished. Typical decay rates for sunspots are in the range from 10 – 180 Mm^2 day^{-1} , as discussed in many studies (e.g., Bumba 1963; Moreno-Insertis & Vázquez 1988; Martínez Pillet et al. 1993; Hathaway & Choudhary 2008), and in the observed active

Table 1. Growth and decay rates for area and magnetic flux.

Area	Growth [Mm^2 day^{-1}]	Decay [Mm^2 day^{-1}]
Photometric	46.6	23.5
		13.9
Magnetic	226.4	99.2
		97.3
Magnetic flux	**Growth [Wb day^{-1}]**	**Decay [Wb day^{-1}]**
Total	2.02	0.44
Positive	1.02	0.24
Negative	1.01	0.20

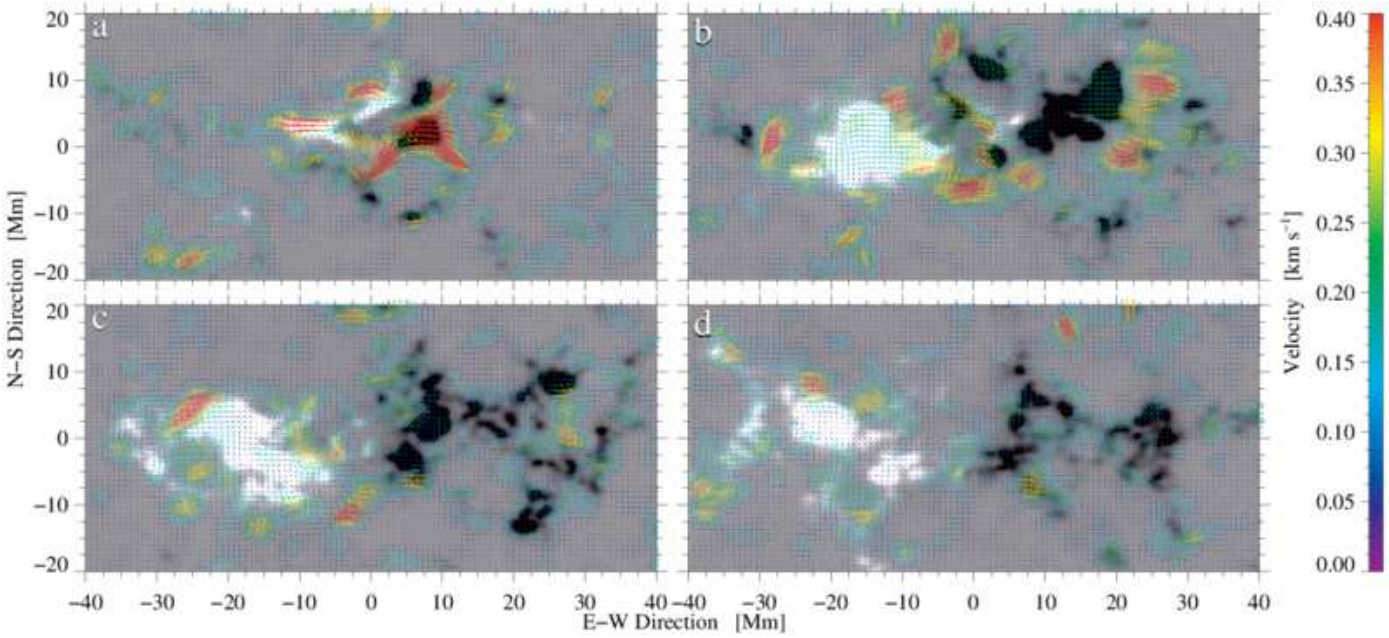

Fig. 6. Horizontal plasma velocities measured with DAVE for two-hour time-series of 45-second HMI magnetograms depicting the four evolutionary stages of the region: (a) 15:30 – 17:30 UT on July 17, (b) 08:00 – 10:00 UT on July 18, (c) 00:00 – 02:00 UT on July 19, and (d) 21:30 – 23:30 UT on July 19. Color-coded vectors (best seen when zooming in in the on-line version, and red indicates a flow speed in excess of 0.4 km s^{-1}) are superposed onto a time-averaged magnetogram covering the respective time-series.

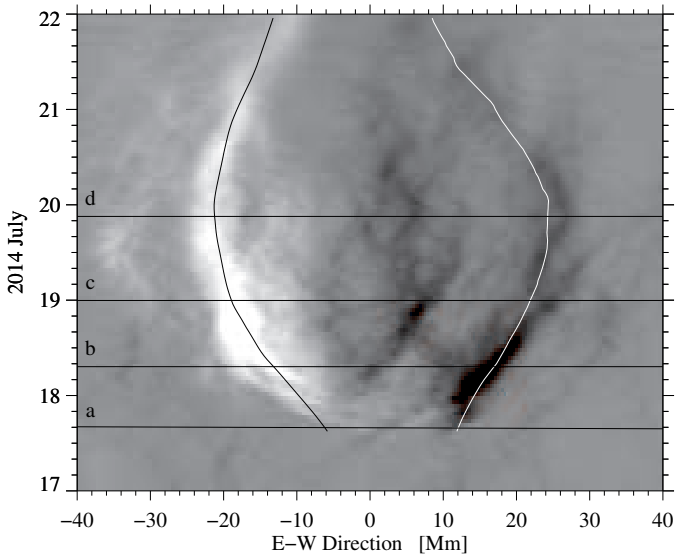

Fig. 5. Space-time diagram collating five days (July 17 – 21) of HMI magnetograms. The magnetic field strength is scaled between ±100 G. The white and black curves trace the location of the extrema of negative and positive polarities over five days. The black horizontal lines indicate the four stages discussed in Sect. 3.2

region with pores the decay rate is still within this range. Rucklidge et al. (1995) observed an overlap between the radii of large pores and small spots. This overlap is a consequence of a convective mode that sets in suddenly and rapidly when the inclination of the photospheric magnetic field exceeds some critical value. As a result, a filamentary penumbra is formed; this process is not observed in our dataset.

Additionally, we computed the magnetic area using a binary mask based on HMI LOS magnetograms. The magnetic area is 4 – 5 times larger than the photometric area (note the two different scales in the left panel of Fig. 4). However, it follows the same trend as the photometric area during the decay phase, which again has two stages, but shifted by about half a day. The growth rate is 226.4 Mm^2 day^{-1}, which is five times the photometric growth rate. The decay rates are very similar 99.2 Mm^2 day^{-1} and 97.3 Mm^2 day^{-1} for the first and second half, respectively, in contrast to the photometric decay rates. The growth rate is faster than the corresponding decay rates (e.g., Verma et al. 2012). As the photometric area approaches zero, magnetic structures become smaller: first dark pores shrink, then they developed into dark magnetic knots (Beckers & Schröter 1968) with sizes smaller than a granule, before dispersing as small-scale bright points (Berger et al. 1995) in regions of abnormal granulation (de Boer & Kneer 1992). The spatial resolution of HMI magnetograms is insufficient to detect magnetic knots or even bright points, that is, the magnetic filling factor in combination with the spatial resolution affects the time when the photometric decay rate reaches zero. Magnetic flux will still be present at this time, so that afterward the development of the active region is governed by the magnetic decay rate.

The growth rates of the magnetic flux are 2.02, 1.02, and 1.01 $\times 10^{13}$ Wb day^{-1} for the total, positive, and negative flux, respectively. The positive and negative flux showed a monotonous rise until the middle of July 18. The growth rates for positive and negative flux are virtually identical. The flux growth rates agree with the result presented by Otsuji et al. (2011). The decay rates of the magnetic flux are 4 – 5 times lower than the growth rates and amounted to 0.44, 0.24, and 0.20 $\times 10^{13}$ Wb day^{-1} for the total, positive, and negative flux, respectively. The decay rates for this small region with pores are in agreement with Kubo et al. (2008), who found a decay rate of about 0.67×10^{13} Wb day^{-1} in a decaying active region. We list all the growth and decay rates in Table 1.

An important evolutionary feature describing the emergence of an active region is the rate at which the two polarities separate. To gain insight into the overall motion of polarities, we created a

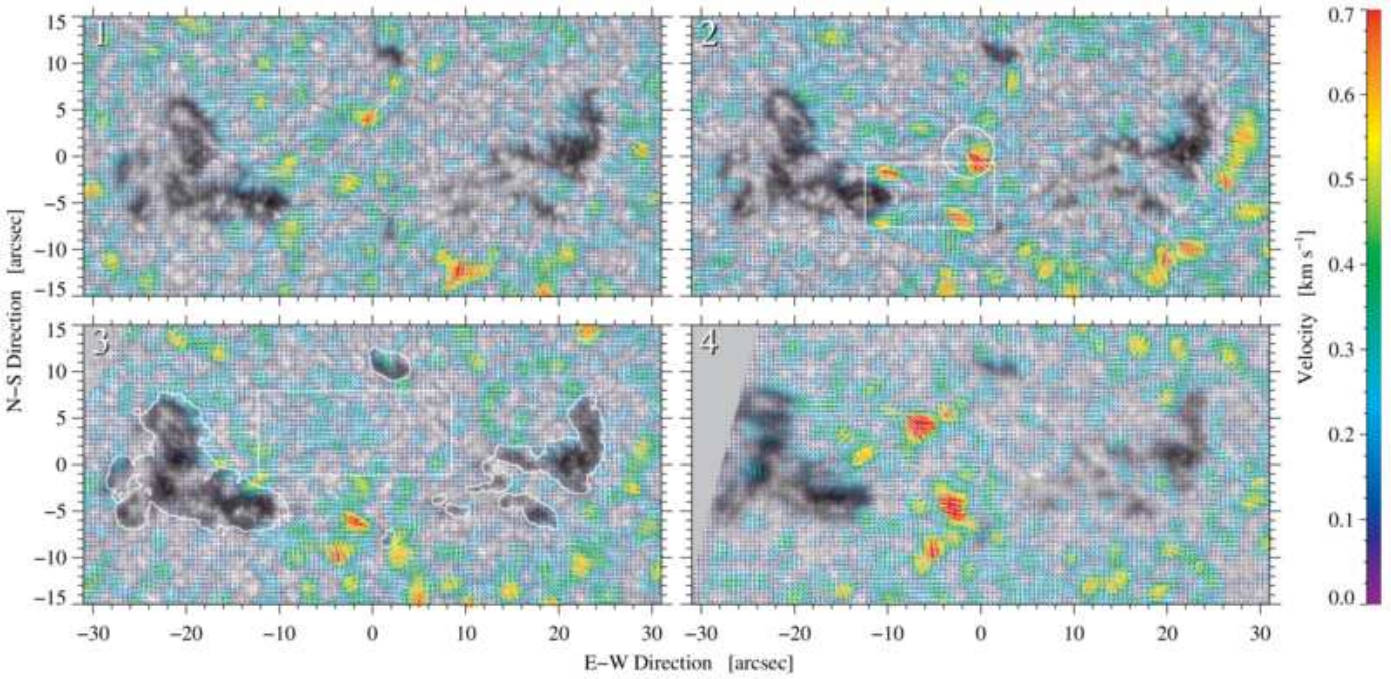

Fig. 7. Horizontal flow field around active region NOAA 12118 computed using GREGOR blue continuum images. Color-coded vectors (best seen when zooming in in the on-line version and red indicates a flow speed in excess of 0.7 km s^{-1}) are superposed onto the first image of the respective time-series. The region is rotated for better display such that its longest axis is horizontal. The white circle in panel (2) indicates a large, elongated, rapidly expanding granule (see Fig. 9). The white rectangle in panel (2) marks the diverging feature present in all panels but it is strongest in panel (2). The white contour lines and rectangle in panel (3) refer to the regions that are used to characterize the horizontal flow speed for various features (see Fig. 8 and Table 3).

Table 2. Parameters describing the horizontal plasma velocities shown in the four panels of Fig. 6.

	$\bar{v}$ [km s^{-1}]	$v_{\rm med}$ [km s^{-1}]	v_{10} [km s^{-1}]	$v_{\rm max}$ [km s^{-1}]	σ_v [km s^{-1}]
Panel 'a'	0.10	0.07	0.23	0.77	0.10
Panel 'b'	0.12	0.10	0.26	0.55	0.10
Panel 'c'	0.11	0.08	0.20	0.51	0.07
Panel 'd'	0.09	0.07	0.17	0.45	0.06

Note: $\bar{v}$ denotes the mean, $v_{\rm med}$ the median, v_{10} the 10$^{\rm th}$ percentile, $v_{\rm max}$ the maximum, and σ_v the standard deviation of the horizontal plasma velocities.

space-time diagram (Fig. 5) encompassing the five days of HMI magnetograms. Since the two major polarities are horizontally aligned along the E-W direction, the images corrected for geometrically foreshortening are averaged along the vertical axis, that is, along the N-S direction. The complete evolution of the active region is thus represented in just one diagram. We computed the maximum and minimum of the positive and negative polarities for each point in time and represent them as black and white curves, which create a leaf-like structure.

Immediately when the two polarities appeared on the surface, they started to move apart, reaching maximum separation, and shortly after began to approach each other. The branches of the two polarities have multiple barbs at their inner sides, indicating coalescence of same-polarity features. The small negative-polarity branch in the center represents the third pore, which spread out while decaying . The maximum separation is 45.6 Mm on July 20 at 01:36 UT. We computed the separation velocity for four evolutionary stages during the growth phase of the region. We tagged these four stages as (a) emerging phase 15:30 – 17:30 UT on July 17, (b) maximum phase 08:00 – 10:00 UT on July 18, (c) second peak phase 00:00 – 02:00 UT on July 19, and (d) decaying phase 21:30 – 23:30 UT on July 19. The stages are indicated by arrows in Fig. 4, the four horizontal lines in Fig. 5, and are explained in detail in Sect. 3.2.

In stage (a) the separation rate is 0.26 km s^{-1}, which is the highest of the four stages and signals the rise of magnetic flux tubes to the solar surface. High separation rates are expected (Otsuji et al. 2011). In the growth phase (b) the polarities are separating with 0.22 km s^{-1}. In stage (c) the separation rate decreased to 0.07 km s^{-1}. Toward the last stage (d), the separation rate reaches its lowest value of 0.02 km s^{-1}, which marks the point when the separation of the polarities stops. The overall separation rate follows the trend discussed in Brants & Steenbeek (1985), Otsuji et al. (2011), and Toriumi et al. (2012): fast separation in the beginning and then slowing down while the region expands. Typical separation rates presented in these studies cover the range of 0.3 – 2.4 km s^{-1}. The highest separation rate for the EFR in active region NOAA 12118 lies below this range. This EFR does not follow the trend that the separation rate is higher for flux tubes containing less magnetic flux, as Otsuji et al. (2011) concluded from a statistical study of 101 EFRs. Finally, another peculiarity concerns the almost identical separation and shrinking rates as the active region grows and decays.

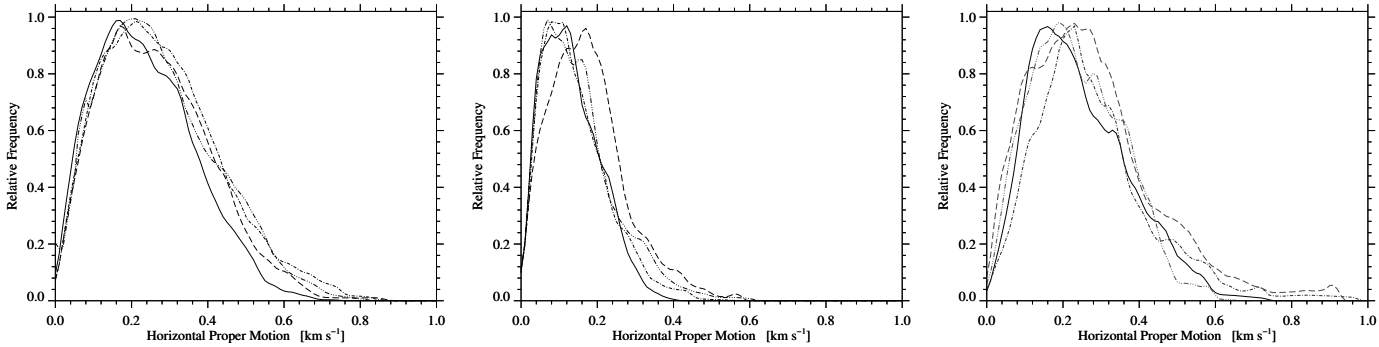

Fig. 8. Relative frequency distributions of horizontal proper motions for granulation (*left*), pores (*middle*), and granulation in the central region between the two major pores of opposite polarity (*right*). The distributions for LCT panels (1)−(4) are depicted as solid, dash-dotted, dash-dot-dotted, and long dashed lines, respectively.

This leaves the impression that a connected flux system rises and, starting at 02:30 UT on July 20, submerges as a whole.

3.2. Magnetic horizontal plasma velocity

We used time-series of HMI magnetograms as input to compute horizontal plasma velocities with DAVE for four evolutionary stages of the region. These stages are marked in Figs. 4 and 5 by black arrows labeled a to d. The averaged horizontal plasma velocities are shown in Fig. 6 as rainbow-colored arrows overlaid on time-averaged (two hours) magnetograms with a FOV of 80 Mm × 40 Mm. We created time-lapse movies to examine changes in the horizontal plasma velocities related to flux emergence in detail.

In phase (a) when the active region is rising to the solar surface, we see strong motions along the horizontal central line pushing the two main patches of opposite polarities rapidly apart. The horizontal plasma velocities are stronger for the negative-polarity region. The central part of the region, within ±5 Mm from the center coordinate (0 Mm, 0 Mm), is dominated by mixed polarities, and coherent motions are absent. Weak swirling motion patterns are present in the southern part of the region, for example, at coordinates (10 Mm, −10 Mm), as is evident in the time-averaged velocity vectors shown in Fig. 6.

The region grows rapidly until July 18, when the fast expansion starts to slow down in phase (b). The magnetic flux in the two major pores P1 and N1 has become very compact. This flux concentration occurred about half a day later for the positive-polarity pore P1. We observe stronger proper motions at the borders of the main flux patches P1 and N1. DAVE picks up the strongest outward motions to the east of the positive polarity P1 and to the west of the negative polarity N1. These strong outward flows around major polarities are vaguely reminiscent of moat flows (Sheeley 1972; Meyer et al. 1974), although they are not symmetric around the magnetic features, and penumbrae are absent. The dominant polarity patches also move apart as a whole. However, the unidirectional flow speed inside the confines of the pores is lower than the external horizontal plasma velocities. The mixed polarities in the active region are the locations of flux cancellation, whereas the dominant positive and negative polarity patches P1 and N1 are locations of flux coalescence, which is also noticeable in the space-time diagram depicted in Fig. 5. Compared to the bulk velocities of major flux concentrations (averaged over the magnetic area of the two major flux patches P1 and N1), the mixed polarity patches have high horizontal plasma velocities, which are still multi-directional.

Table 3. Parameters describing the horizontal proper motions computed from averaging all four LCT maps (Fig. 7) for granulation (*top*), pores (*middle*), and granulation in between the pores P1 and N1 of opposite polarities (*bottom*).

$\overline{v}$ [km s^{-1}]	$v_{\rm med}$ [km s^{-1}]	v_{10} [km s^{-1}]	$v_{\rm max}$ [km s^{-1}]	σ_v [km s^{-1}]
0.27	0.26	0.47	0.83	0.15
0.16	0.14	0.28	0.55	0.09
0.26	0.24	0.46	0.83	0.14

In phase (c) the separation of the two polarities slows down even further and almost comes to a halt. During this period, the negative polarity has started to disperse and is fragmented, while the positive polarity patch is more compact. However, both patches are now clearly separated, and the central part is devoid of any mixed polarities. The overall velocity pattern is patchy, but a strong eastward motion in the positive-polarity is still observed. The upper part of the negative-polarity patch still shows expanding motions. In general, the flow speed is lower than in phases (a) and (b).

Phase (d) marks the decay phase of the active region evolution. The magnetic area of both polarities is smaller and more fragmented. The negative polarities remain as small-scale flux elements. The horizontal plasma velocities are reduced in the area covered by these small-scale magnetic elements, and the horizontal plasma velocity pattern becomes more random for the more compact positive polarity patch. In general, the horizontal plasma velocities are no longer coherent, and the strongest velocities are found outside the active region.

To characterize velocities computed with DAVE, we present descriptive parameters in Table 2. The frequency distributions (not shown) for all four evolutionary stages are narrow with a high velocity tail. The mean velocity $\overline{v} \approx 0.10$ km s^{-1} is in agreement with the quiet-Sun values presented by Diercke (2014) and Kuckein et al. (2016) for small-scale magnetic elements along an extended filament channel.

3.3. Horizontal proper motions

Using blue continuum images obtained with GREGOR/BIC, we examined the high-resolution spatial and temporal evolution of horizontal proper motions with LCT (Fig. 7). We have four time-

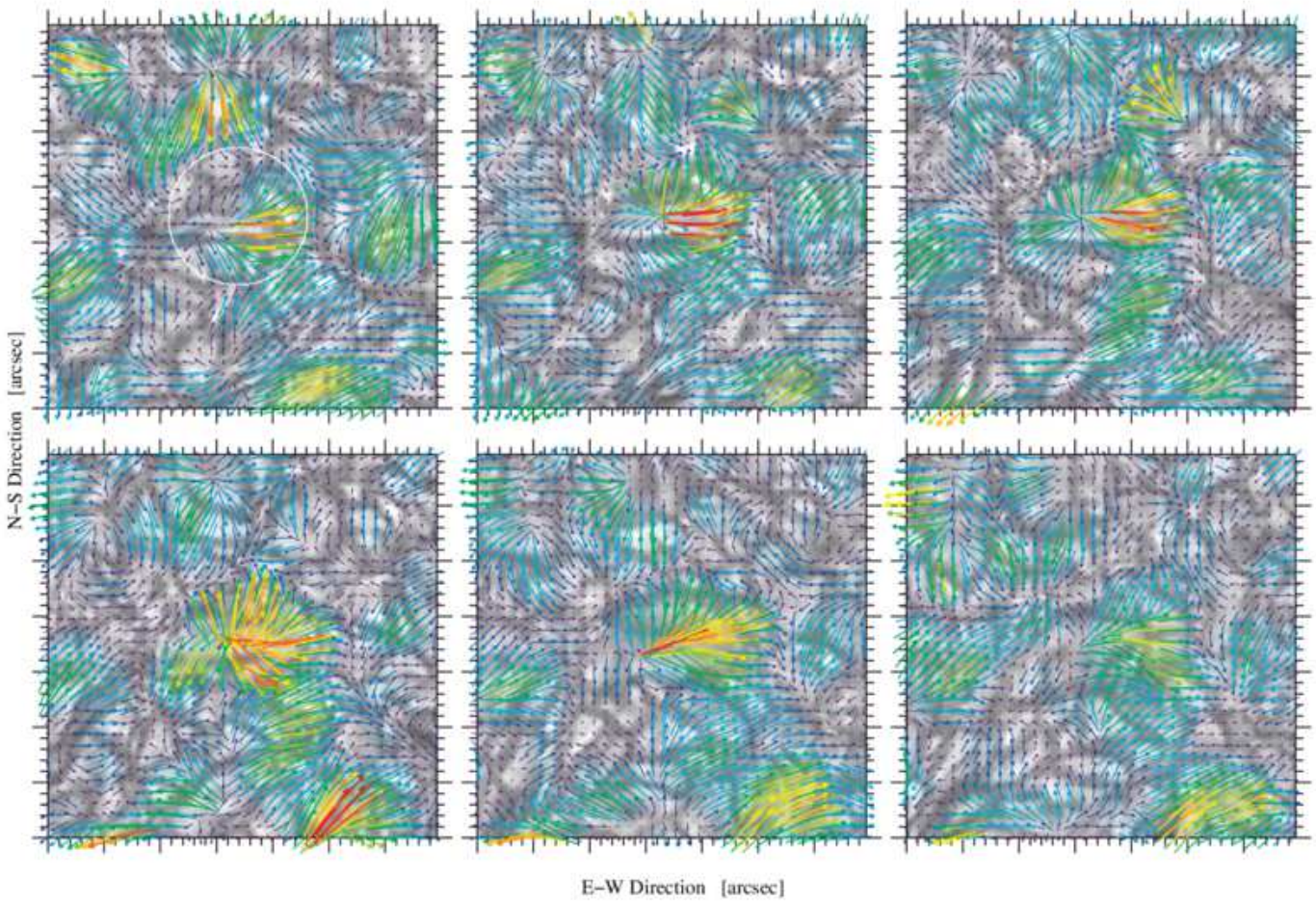

Fig. 9. Cutouts of 14″×14″ from blue continuum images (*right to left*) with a rapidly expanding granule in the center at six evolutionary stages from the second time-series starting at 08:36 UT on July 18. Color-coded 5-minute-averaged velocity vectors (red indicates a flow speed in excess of 0.7 km s^{-1}) are superposed onto the first image of the respective time-series. The white circle in the first panel marks the location of the rapidly expanding granule.

series on 2014 July 18 starting at (1) 07:56 UT, (2) 08:36 UT, (3) 09:13 UT, and (4) 10:09 UT. These times are centered on the active region at maximum growth. The FOV is rotated to match the orientation of the HMI continuum images and LOS magnetograms. The overall appearance of the LCT flow pattern is very different from those computed with DAVE. However, the LCT and DAVE maps cannot be compared because they sample different flow fields.

In all four panels we have two large conglomerates of pores (P1 and N1 and one smaller pore N2 at the top. In all four time-series the eastern pore P1 is growing, whereas the western pore N1 continuously decays. By the fourth time-series the smaller pore N2 also begins to decay. The average area of about 82.2 Mm^2 and 34.3 Mm^2 for P1 and N1, respectively, lies on the higher end of the values computed in the statistical study of pores by Verma & Denker (2014). Few flow patterns remain the same in all four panels. A recurring pattern is, for example, the central region between P1 and N1, which contains abnormal granulation and is the site of many rapidly expanding granules. A moat-like outward motion encircles N1 giving the impression that the pore is in the center of a larger supergranular cell. In addition, the dark features with strong magnetic fields have reduced LCT proper motions.

Large rapidly expanding granules, which are often elongated, are present in all time-series across the entire FOV, but they are more frequent in the central part of the active region. Some of these granules reach a length of 6″ and a width of 2″, whereas normal granules are smaller and more circular with diameters of around 2″ (Hirzberger et al. 1997). The circle in Fig. 7 marks the location of one such granule in close proximity to a magnetic bipole, which is indicative of an Ω loop rising through the photosphere. In the absence of magnetograms with high spatial resolution, it is difficult to find an alignment between the major axes of the elongated granules and the orientation of the magnetic field. Size, elongation, and location of this particular kind of granules suggest an association with emerging flux rather than pointing to extreme cases of regular exploding granules (Namba 1986; Rast 1995; Hirzberger et al. 1999). However, in both cases divergence centers mark the location of granules associated with flux emergence (Ortiz et al. 2014) and regular exploding granules (e.g., Bonet et al. 2005). In consequence, we prefer the term ‘rapidly expanding’ over ‘exploding’ granules in this study related to flux emergence.

All pores contain multiple umbral dots (cf., Sobotka & Hanslmeier 2005) and around the two major pores finger-like structures intrude into the dark core (cf., Scharmer et al. 2002; Bellot Rubio et al. 2008), but the pores never developed penum-

brae. In all four panels around 10 – 20 short-lived magnetic knots with a size smaller than one second of arc appear and disappear in the central part of the active region between P1 and N1. The central part is characterized by horizontal channels of aligned intergranular lanes connecting the two magnetic polarities (cf., Strous 1995; Strous & Zwaan 1999). Both P1 and N1 exhibit inflows from the central part of the active region. In addition to the inflows, N1 shows strong outward flows at its western periphery, in particular in panel (2).

Panel (2) shows very similar morphological and flow properties as panel (1). Around N1 the moat-like outward motion is stronger, with large granules fragmenting near its border. Horizontal alignment of granules extending between two polarities is present, but not as pronounced as in panel (1). The most striking LCT flow feature in panel (2) is the strong divergence region with flow vectors curling around the southwestern part of P1. This divergence pattern is strongest in panel (2), but it is present in all panels. We marked it with a white rectangle in panel (2). This diverging flow pattern suggests persistent upwelling and emergence of magnetic flux.

In panel (3) the overall flow pattern remains the same as in the previous panel. However, the magnitude of the velocity is lower. The inflows and outflows from the inner and outer parts of pores are still present. The strong divergence feature to the southwest of P1 still exists. Various rapidly expanding granules are present, but they are not as large as in panels (1) and (2). The LCT flow field in panel (4) follows the flow pattern in the previous panels. In all four panels, the interior of pores does not have uniform and ordered flow vectors as seen in the DAVE maps. Although a few dominant flow features are the same in all panels, the flow field evolves significantly over half an hour. To quantitatively infer the properties of the central region with granulation, we computed relative frequency distributions for all four panels, which we discuss in Sect. 3.4.

Similar to the space-time diagram of HMI magnetograms, we created a space-time diagram for 2.75 hours using four time-sequences (not shown). The computed separation speeds are for panels (1) 0.61 km s^{-1}, (2) 0.34 km s^{-1}, (3) 0.11 km s^{-1}, and (4) 0.36 km s^{-1}. These separation speeds are higher than the values derived from the HMI space-time diagram. The difference could arise from the fact that we tracked intricate details within pores in the blue continuum images, whereas in magnetograms we observe these pores as large polarity patches. Small changes in the high-resolution images can lead to large differences in the space-time diagrams.

3.4. Characteristics of horizontal proper motions

To gain insight into the statistical properties of the LCT velocities in different solar features we computed relative frequency distributions using binary masks. We depict these masks in the third panel of Fig. 7, where the contours mark pores and the central region with granulation. The respective distributions are compiled in Fig. 8 and Table 3, which includes the various parameters of these distributions. The four distributions for granulation are broad, but without a high-velocity tail and with mean velocities extending between $\overline{v}$ = 0.24 – 0.28 km s^{-1}. The corresponding standard deviation values are within the limits of σ_v = 0.13 – 0.16 km s^{-1}. These values for granulation reach only about half the numerical values presented by Verma & Denker (2011) based on Hinode G-band images, but they are closer to the values $\overline{v}$ = 0.35 ± 0.21 km s^{-1} of Verma & Denker (2012).

The lower granular flow speed might result from the proximity to strong magnetic flux concentrations. The velocity distributions of the central region with granulation differs from the distribution for granulation per se. The distributions are narrower and have a high-velocity tail. However, the mean velocity remains roughly the same. The high-velocity tail is attributed to the presence of many rapidly expanding granules. The distributions of pores are narrow. The mean values cover the range between $\overline{v}$ = 0.14 – 0.18 km s^{-1} with standard deviation of σ_v = 0.07 – 0.10 km s^{-1}. Even though somewhat lower, the results agree with values computed by Verma & Denker (2011, 2012).

3.5. Horizontal proper motions associated with rapidly expanding granules

Taking advantage of the high spatial resolution provided by the GREGOR solar telescope, we zoomed-in to scrutinize the fine details on the solar surface. One of the emerging active region's dynamical characteristics are large elongated granules (Rezaei et al. 2012; Guglielmino et al. 2010). Various stages of an expanding granule are presented in Fig. 9. The FOV of 14″ × 14″ is centered on the granule. The six panels are separated by 5 min in time and thus cover a period of 30 min. The LCT velocities are averaged over 5 min. The divergence was also computed using the time-averaged velocity components (not shown).

The central region with granulation has a positive divergence from the beginning. However, the magnitude first increases with time before fading away and spreading after about 15 min. The strong divergence center is a well -observed property of exploding granules (e.g., Hirzberger et al. 1999) as well as rapidly expanding granules in regions of flux emergence (Rezaei et al. 2012). The large size and aspect ratio in combination with the appearance of a dark central lane within the upwelling plasma favor the latter scenario. The mean divergence in the rapidly expanding granule (depicted by the white circle in Fig. 9) ranges from $2.0\times10^{-3} - 6.3\times10^{-4}$ s^{-1}. The corresponding velocity vectors trace the full extent of the expanding granule. The strong divergence region is surrounded by a negative divergence ring, which closely follows the intergranular boundary. The length and width of the granule are about 3.6″ and 1.6″, respectively, which agrees with previous observations (Namba 1986). The mean velocity within the rapidly expanding granule for the first panel is 0.40 km s^{-1}, which increases to 0.72 km s^{-1} for the fourth panel and decreases to 0.34 km s^{-1} for the sixth panel, which is consistent with recent results of Palacios et al. (2012). The highest velocity is encountered in the fifth panel and amounts to 1.25 km s^{-1}. This value is much lower than the one of about 4 km s^{-1} given by Guglielmino et al. (2010), which can be easily explained by the very narrow sampling window (FWHM < 0.2″) employed by these authors, however. Verma & Denker (2011) discussed the dependence of LCT results on sampling window properties and averaging times in detail.

4. Summary and conclusions

We presented one of the data sets taken during the early science phase of the GREGOR solar telescope. The high-resolution images of active region NOAA 12118 captured with BIC allowed us to study the morphological and flow properties of a small active region. HMI continuum images and magnetograms provided valuable magnetic information. The major findings of this study can be summarized as follows.

The evolution of NOAA 12118 started with the emergence of new flux on the solar surface followed by flux coalescence. In the emerging phase, many mixed-polarity features are in between the two major pores. This leads to a complex magnetic

neutral line, which simplified with time. Even though the pores never developed penumbrae, we observed strong outward flows, which indicate the expansion of the active region when the pores push through the surrounding plasma. The alternative explanation that the outflows give the impression of a partial moat flow is less convincing in the absence of Evershed flow (cf., Vargas Domínguez et al. 2008, 2010), Evershed clouds (Cabrera Solana et al. 2006), and moving magnetic features (MMFs, Harvey & Harvey 1973) as signatures of an extended radial flow system. Ultimately, high-resolution spectroscopic observations are needed to elucidate the origins of outflows. The growth rates for photometric area, magnetic area, and magnetic flux are about twice as high as the corresponding decay rates, which is consistent with previous studies (Verma et al. 2012). The computed magnetic area is four to five times larger than the photometric area.

The HMI magnetograms were used to compute the horizontal plasma velocities and blue continuum images of GREGOR provided the horizontal proper motions for the active region. However, the flow patterns are different and poorly correlated on account of several factors. First, the horizontal plasma velocities (DAVE) and plasma motions (LCT) track different, only weakly related physical processes (Welsch et al. 2007). Second, in the active region magnetic features are not advected by surface flows but rather by subsurface phenomena (Zhao et al. 2010). Third, the difference in the spatial resolution plays a significant role. The high-resolution of GREGOR images allow following flows due to motion and distortion of individual granules, which is not possible in HMI magnetograms.

The central region between the two major pores contained abnormal granulation and many large, elongated, and rapidly expanding granules. This central region also had different relative frequency distributions for granulation with high-velocity tails. The high-resolution image sequences facilitated precise LCT measurements of horizontal proper motions, and the results agree well with previous LCT studies (Verma & Denker 2011; Verma et al. 2012; Verma & Denker 2012). Even the intricate details of the flow fields belonging to a large, rapidly expanding granule are well captured by the LCT. Using the space-time diagram, we inferred the separation rates of the two major pores. The expansion and shrinking of the active region exhibit symmetries with respect to separation velocities (about ± 0.25 km s^{-1}) and length of the evolutionary phases (five days). The separation rates computed agree with previous work.

The leaf-like structure that traced both polarities in the space-time diagram indicates an atypical behavior of active regions, where flux dispersal commonly characterizes the decay process. We speculate that the morphology of main pores is the reason because they never developed penumbrae and as a consequence never produced an Evershed flow (Evershed 1909). The lack of a fully developed penumbra results in the absence of a uniform moat flow. In addition, the surroundings of the pores are void of any MMFs (Harvey & Harvey 1973), which play a key role in the decay of an active region by magnetic flux erosion. The region was also exceptional because the trailing part remained more stable than the leading part, which disintegrated first. Hence, the temporal evolution of this active region is consistent with the emergence of monolithic flux tube and its subsequent submergence, which leads to the characteristic leaf-like structure in the space-time diagram.

The evolution of the active region presented in this study closely follows the evolutionary path outlined by Otsuji et al. (2011), Centeno (2012), and Toriumi et al. (2012). In the present study, the two main pores have high separation rates in the beginning. Once the region reaches its maximum flux and size by the end of July 18, the separation rate slows down. This trend closely resembles the observation of an EFR by Toriumi et al. (2012) and is consistent with numerical simulations by Stein et al. (2011). Similar to observations of Centeno (2012), the region in our study has elongated rapidly expanding granules appearing between the two main polarities, along with flux cancellation. These features are also seen in the simulation by Stein et al. (2011), where the emerging magnetic field distorts the granules, stretching them in the direction of the horizontal field. In numerical simulations of Cheung et al. (2010) the horizontal expansion of magnetic plasma is prevalent while rising. The emergence of small magnetic features is followed by their coalescence. We also noted the same pattern, where the initial appearance of the magnetic features is followed by the growth of pores and their coalescence. In the simulated active region the mean flow pattern was radially outward, which we only observed at the leading and to a lesser extent at the trailing edges of the active region, whereas inflows into pores were sometimes observed in the interior of the active region.

In the future, we will combine spectropolarimetric observations of the GFPI and the GREGOR Infrared Spectrograph (GRIS, Collados et al. 2012). High-resolution imaging along with precision infrared spectropolarimetry will allow us to follow the evolution of flows as well as the magnetic evolution of active regions from the photosphere to the chromosphere. Simultaneous observations with the Hinode (Kosugi et al. 2007) and the Interface Region Imaging Spectrograph (IRIS, De Pontieu et al. 2014) will complement the ground-based observations, along with synoptic data from SDO. Detailed information of flows and magnetic fields during the emerging phase are still needed to better constrain numerical simulations (Rempel & Cheung 2014).

Acknowledgements. The 1.5-meter GREGOR solar telescope was build by a German consortium under the leadership of the Kiepenheuer-Institut für Sonnenphysik in Freiburg with the Leibniz-Institut für Astrophysik Potsdam, the Institut für Astrophysik Göttingen, and the Max-Planck-Institut für Sonnensystemforschung in Göttingen as partners, and with contributions by the Instituto de Astrofísica de Canarias and the Astronomical Institute of the Academy of Sciences of the Czech Republic. SDO HMI and AIA data are provided by the Joint Science Operations Center – Science Data Processing. MS is supported by the Czech Science Foundation under the grant 14-0338S. CD is supported by the German Science Foundation (DFG) under grant DE 787/3-1. This study is supported by the European Commission's FP7 Capacities Programme under the Grant Agreement number 312495. SJGM is grateful for financial support from the Leibniz Graduate School for Quantitative Spectroscopy in Astrophysics, a joint project of AIP and the Institute of Physics and Astronomy of the University of Potsdam (UP).

References

Beckers, J. M. & Schröter, E. H. 1968, Sol. Phys., 4, 142
Bello González, N. & Kneer, F. 2008, A&A, 480, 265
Bellot Rubio, L. R., Tritschler, A., & Martínez Pillet, V. 2008, ApJ, 676, 698
Bendlin, C., Volkmer, R., & Kneer, F. 1992, A&A, 257, 817
Berger, T. E., Schrijver, C. J., Shine, R. A., et al. 1995, ApJ, 454, 531
Berkefeld, T., Schmidt, D., Soltau, D., von der Lühe, O., & Heidecke, F. 2012, AN, 333, 863
Berkefeld, T., Soltau, D., Schmidt, D., & von der Lühe, O. 2010, Appl. Opt., 49, G155
Bethge, C., Peter, H., Kentischer, T. J., et al. 2011, A&A, 534, A105
Bonet, J. A., Márquez, I., Muller, R., Sobotka, M., & Roudier, T. 2005, A&A, 430, 1089
Brants, J. J. & Steenbeek, J. C. M. 1985, Sol. Phys., 96, 229
Bumba, V. 1963, Bull. Astron. Inst. Czech, 14, 91
Cabrera Solana, D., Bellot Rubio, L. R., Beck, C., & del Toro Iniesta, J. C. 2006, ApJL, 649, L41
Centeno, R. 2012, ApJ, 759, 72

Cheung, M. C. M., Rempel, M., Title, A. M., & Schüssler, M. 2010, ApJ, 720, 233
Collados, M., López, R., Páez, E., et al. 2012, AN, 333, 872
Couvidat, S., Schou, J., Shine, R. A., et al. 2012, Sol. Phys., 275, 285
de Boer, C. R. & Kneer, F. 1992, A&A, 264, L24
De Pontieu, B., Title, A. M., Lemen, J. R., et al. 2014, Sol. Phys., 289, 2733
Denker, C., Balthasar, H., Hofmann, A., Bello González, N., & Volkmer, R. 2010, in Proc. SPIE, Vol. 7735
Denker, C., Johannesson, A., Marquette, W., et al. 1999, Sol. Phys., 184, 87
Denker, C., von der Lühe, O., Feller, A., et al. 2012, AN, 333, 810
Diercke, A. 2014, Bachelor thesis, Universität Potsdam, Germany
Druckmüller, M. 2013, ApJSS, 207, 25
Evershed, J. 1909, MNRAS, 69, 454
Gallagher, P. T., Moon, Y.-J., & Wang, H. 2002, Sol. Phys., 209, 171
Guglielmino, S. L., Bellot Rubio, L. R., Zuccarello, F., et al. 2010, ApJ, 724, 1083
Hale, G. E., Ellerman, F., Nicholson, S. B., & Joy, A. H. 1919, ApJ, 49, 153
Harvey, K. & Harvey, J. 1973, Sol. Phys., 28, 61
Hathaway, D. H. & Choudhary, D. P. 2008, Sol. Phys., 250, 269
Hirzberger, J., Bonet, J. A., Vázquez, M., & Hanslmeier, A. 1999, ApJ, 527, 405
Hirzberger, J., Vázquez, M., Bonet, J. A., Hanslmeier, A., & Sobotka, M. 1997, ApJ, 480, 406
Kentischer, T. J., Bethge, C., Elmore, D. F., et al. 2008, in Proc. SPIE, Vol. 7014, Ground-Based and Airborne Instrumentation for Astronomy II, ed. I. S. McLean & M. M. Casali, 13
Knox, K. T. & Thompson, B. J. 1974, ApJL, 193, L45
Kosugi, T., Matsuzaki, K., Sakao, T., et al. 2007, Sol. Phys., 243, 3
Kubo, M., Lites, B. W., Shimizu, T., & Ichimoto, K. 2008, ApJ, 686, 1447
Kubo, M., Shimizu, T., & Lites, B. W. 2003, ApJ, 595, 465
Kuckein, C., Verma, M., & Denker, C. 2016, A&A, 589, A84
Labeyrie, A. 1970, A&A, 6, 85
Leenaarts, J., Rutten, R. J., Carlsson, M., & Uitenbroek, H. 2006, A&A, 452, L15
Lemen, J. R., Title, A. M., Akin, D. J., et al. 2012, Sol. Phys., 275, 17
Lites, B. W., Skumanich, A., & Martínez Pillet, V. 1998, A&A, 333, 1053
López Fuentes, M. C., Demoulin, P., Mandrini, C. H., & van Driel-Gesztelyi, L. 2000, ApJ, 544, 540
Luoni, M. L., Démoulin, P., Mandrini, C. H., & van Driel-Gesztelyi, L. 2011, Sol. Phys., 270, 45
Martínez Pillet, V., Moreno-Insertis, F., & Vázquez, M. 1993, A&A, 274, 521
Meyer, F., Schmidt, H. U., Wilson, P. R., & Weiss, N. O. 1974, MNRAS, 169, 35
Moreno-Insertis, F. & Vázquez, M. 1988, A&A, 205, 289
Namba, O. 1986, A&A, 161, 31
Ortiz, A., Bellot Rubio, L. R., Hansteen, V. H., de la Cruz Rodríguez, J., & Rouppe van der Voort, L. 2014, ApJ, 781, 126
Otsuji, K., Kitai, R., Ichimoto, K., & Shibata, K. 2011, PASJ, 63, 1047
Palacios, J., Blanco Rodríguez, J., Vargas Domínguez, S., et al. 2012, A&A, 537, A21
Parker, E. N. 1955, ApJ, 121, 491
Puschmann, K. G., Denker, C., Kneer, F., et al. 2012, AN, 333, 880
Puschmann, K. G., Kneer, F., Seelemann, T., & Wittmann, A. D. 2006, A&A, 451, 1151
Rast, M. P. 1995, ApJ, 443, 863
Rempel, M. & Cheung, M. C. M. 2014, ApJ, 785, 90
Rezaei, R., Bello González, N., & Schlichenmaier, R. 2012, A&A, 537, A19
Rucklidge, A. M., Schmidt, H. U., & Weiss, N. O. 1995, MNRAS, 273, 491
Scharmer, G. B., Gudiksen, B. V., Kiselman, D., Löfdahl, M. G., & Rouppe van der Voort, L. H. M. 2002, Nature, 420, 151
Scharr, H. 2007, in Lecture Notes in Computer Sciences, Vol. 3417, Complex Motion, ed. B. Jähne, R. Mester, B. Barth, & H. Scharr (Berlin: Springer), 14–29
Scherrer, P. H., Schou, J., Bush, R. I., et al. 2012, Sol. Phys., 275, 207
Schmidt, W., von der Lühe, O., Volkmer, R., et al. 2012, AN, 333, 796
Schou, J., Scherrer, P. H., Bush, R. I., et al. 2012, Sol. Phys., 275, 229
Schuck, P. W. 2005, ApJL, 632, L53
Schuck, P. W. 2006, ApJ, 646, 1358
Sheeley, Jr., N. R. 1972, Sol. Phys., 25, 98
Sobotka, M. & Hanslmeier, A. 2005, A&A, 442, 323
Solanki, S. K. 2003, A&ARev, 11, 153
Stein, R. F., Lagerfjärd, A., Nordlund, Å., & Georgobiani, D. 2011, Sol. Phys., 268, 271
Strous, L. H. 1995, in ESA Special Publication, Vol. 376, Helioseismology, 213–217
Strous, L. H., Scharmer, G., Tarbell, T. D., Title, A. M., & Zwaan, C. 1996, A&A, 306, 947
Strous, L. H. & Zwaan, C. 1999, ApJ, 527, 435
Toriumi, S., Hayashi, K., & Yokoyama, T. 2012, ApJ, 751, 154
Uitenbroek, H. & Tritschler, A. 2006, ApJ, 639, 525
Vargas Domínguez, S., de Vicente, A., Bonet, J. A., & Martínez Pillet, V. 2010, A&A, 516, A91
Vargas Domínguez, S., Rouppe van der Voort, L., Bonet, J. A., et al. 2008, ApJ, 679, 900
Verma, M., Balthasar, H., Deng, N., et al. 2012, A&A, 538, A109
Verma, M. & Denker, C. 2011, A&A, 529, A153
Verma, M. & Denker, C. 2012, A&A, 545, A92
Verma, M. & Denker, C. 2014, A&A, 563, A112
Verma, M., Steffen, M., & Denker, C. 2013, A&A, 555, A136
Volkmer, R., Eisenträger, P., Emde, P., et al. 2012, AN, 333, 816
Wachter, R., Schou, J., Rabello-Soares, M. C., et al. 2012, Sol. Phys., 275, 261
Watanabe, H., Kitai, R., Okamoto, K., et al. 2008, ApJ, 684, 736
Weigelt, G. & Wirnitzer, B. 1983, Opt. Lett., 8, 389
Welsch, B. T., Abbett, W. P., De Rosa, M. L., et al. 2007, ApJ, 670, 1434
Wöger, F. & von der Lühe, O. 2008, in Proc. SPIE, Vol. 7019, Advanced Software and Control for Astronomy II, ed. A. Bridger & N. M. Radziwill, 70191E
Wöger, F., von der Lühe, O., & Reardon, K. 2008, A&A, 488, 375
Xu, Z., Lagg, A., & Solanki, S. K. 2010, A&A, 520, A77
Zhao, J., Kosovichev, A. G., & Sekii, T. 2010, ApJ, 708, 304
Zwaan, C. 1978, Sol. Phys., 60, 213
Zwaan, C. 1985, Sol. Phys., 100, 397